Dense heterogeneous interfaces boost the electrocatalytic oxygen evolution reaction

Shuai Liu [a], Fumin Wang [a], Jiawei Wang [a], Zheng Wang [a], Xinyuan He [a], Tongxue Zhang [a], Zhiwei Zhang [a], Qian Liu [b], Xijun Liu [c], Xubin Zhang [a,*]

[a] School of Chemical Engineering and Technology, Tianjin University, Tianjin 300350, PR China
[b] Institute for Advanced Study, Chengdu University, Chengdu, Sichuan 610106, PR China
[c] School of Resource, Environments and Materials, Guangxi University, Nanning 530004, PR China

ARTICLE INFO

ABSTRACT

Efficient and cost-effective catalysts are essential to drive the oxygen evolution reaction (OER) in sustainable hydrogen production through water splitting. In this study, we introduce an innovative strategy aimed at constructing heterogeneous structure that form abundant $Fe_2O_3/NiSe_2$ interfaces on the FeOOH surface. The resulting catalyst exhibits extraordinary performance with an excellently low overpotential of 169 mV at 10 mA cm^{-2}. Notably, this catalyst also demonstrates impressive long-term stability in alkaline seawater. Compared to traditional heterogeneous catalysts with core-shell structures, $Fe_2O_3/NiSe_2$ possesses a closely heterogeneous interface, which plays a role in modulating the interface electron. Supported by complementary spectroscopy and theoretical calculations, it has been further demonstrated that the distinctive Fe-O-Ni-Se structure can effectively modulate the electronic state of Ni, thereby enhancing the adsorption of oxygen-containing intermediates and facilitating oxygen desorption. Overall, this research presents a promising avenue for enhancing the electrocatalytic performance by amplifying active sites at interfaces.

1. Introduction

Hydrogen (H_2), characterized by its remarkable energy density and sustainability, emerges as an auspicious alternative to conventional fossil fuels. Producing H_2 from methane and other fossil fuels is currently a common way, it unfortunately gives rise to substantial carbon emissions. To tackle these challenges related to carbon emissions, the generation of H_2 through alkaline water splitting is deemed among the most viable pathways for future energy provisioning [1].The key to improving the efficiency of water electrolysis lies in accelerating the oxygen evolution reaction (OER) at the anode, as the OER is more kinetically sluggish than the hydrogen evolution reaction (HER) at the cathode [2,3]. However, RuO_2 and IrO_2, which are commonly used as catalysts, are underperformed of stability despite their scarcity and high cost [4,5]. Therefore, developing efficient and stable non-precious metal catalysts is crucial for accelerating the kinetics of the OER process [6]. Transition metal (Ni, Co, Fe, Mn), with its favorable soil abundance, excellent conductivity, and adjustable electronic structure, has emerged as a promising, economical, and efficient replacement for these

expensive catalysts. Various strategies have been developed for regulating the electronic structure and coordination environment of transition metals, including metal doping [7,8], defect engineering [9], and nonmetallic coordination [10,11].

Transition metal selenides have been widely employed in electrocatalysis owing to their low cost, abundant reserves, and commendable conductivity [12,13]. Nevertheless, the performance of these catalysts is far from satisfactory for unfavorable electron configuration, insufficient exposure of the active sites, and limited stability under harsh operating conditions. To address these issues, heterojunctions composed of transition metal selenides have gained significant attention in recent years [14,15]. These heterojunctions are synthesized by interface engineering, which allows for the promotion of interfacial electron transfer, optimization of the electron distribution at the active site, and influence on the adsorption/desorption of reaction intermediates. For instance, $Fe_3Se_4/FeSe$ [16] and Ni_3Se_4/Ni [17] heterojunctions unveil that the phase boundary of the heterojunction can induce interfacial electron redistribution, forming an optimal electronic structure suitable for adsorption/decomposition of oxygen-containing intermediates. Huang et al.

[18] synthesized heterogeneous $Ni_3Se_4/NiSe_2$ nanorods by adjusting the temperature of selenization. The high surface roughness of these heterojunction nanorods not only increases the active area but also improves the mass transfer efficiency, manifesting superior performance compared to its homogeneous counterpart in urea oxidation reactions. Moreover, in addition to the advantages inherited from the high specific surface area, their excellent electrochemical performance is also attributed to the reinforcement and synergetic effect of multicomponent. Hu's group [19] found that the introduction of atomic interface can reduce the oxidation overpotential of bimetallic Ni and Co active sites, and promote the enhancement of catalytic performance by improving the inherent reactivity of metal atoms and enhancing the synergistic effect between the internal selenides and the surface oxidized substances. However, previous reports have neglected the role of interfacial bonding in regulating the electronic states of different components of heterojunctions. Interface bonding is crucial not only for the interaction between these components but also for the stability of the material due to the typically weak binding energy between these components. Additionally, the reported heterojunctions primarily consist of core-shell structures formed through multi-step synthesis [20–24], resulting in a distribution of sparse interfacial within layers. As a consequence, the limited presence of the interface position severely hampers the optimization of adsorption energy, leading to poor performance in OER. Therefore, the fabrication of catalysts with dense heterogeneous interfaces, especially those incorporating diverse metal cations, represents a notably challenging endeavor that has been scarcely reported.

Herein, we report a simple and feasible strategy for designing efficient and stable OER electrocatalysts. Through one-step selenisation of nickel foam (NF) containing FeOOH, heterojunctions with rich $Fe_2O_3/NiSe_2$ interface are synthesized ($Fe_2O_3/NiSe_2$-FeOOH/NF). The highly hydroxylated FeOOH nanosheets induce a hyper-hydrophilic surface, which increases reactant concentration and improves mass transfer. The enriched $Fe_2O_3/NiSe_2$ interface optimizes the electron distribution in the active site, resulting in a moderate oxidation state of Ni, which enhances the binding energy with oxygen-containing intermediate, thus leading to excellent performance in OER. Specifically, $Fe_2O_3/NiSe_2$-FeOOH/NF demonstrates a low overpotential of 169 mV at the current density of 10 mA cm^{-2}, a small Tafel slope of 31.2 mV dec^{-1}, and a long-period stability of up to 200 hours. Density functional theory (DFT) calculations further reveal that the Gibbs free energy of Ni as active sites in $Fe_2O_3/NiSe_2$ is reduced by approximately 0.13 eV from *O to *OOH compared with $NiSe_2$. Moreover, in-situ Raman spectroscopy confirms the reconstitution of Ni into highly active NiOOH at the lower potential in $Fe_2O_3/NiSe_2$-FeOOH/NF. In conclusion, this work presents a novel strategy for the design of efficient and stable OER electrocatalysts.

2. Experimental section

2.1. Chemicals and materials

Iron nitrate nonahydrate ($Fe(NO_3)_3$ 9 H_2O, 99%), potassium hydroxide (KOH, 90%), urea (CH_4N_2O, 99%), ammonium fluoride (NH_4F, 95%), potash iodide (KI, 99%), Nickel selenide ($NiSe_2$,95%), were purchased from Shanghai Aladdin Chemical Reagent Co., Ltd. Selenium powder (Se, 99.9%) and sodium hydroxide (NaOH, 95%), ferric oxide (Fe_2O_3, 99%), obtained from Shanghai Maclin Biochemical Technology Co., Ltd, Pt/C (40 wt%, Alfa Aesar), Nafion (D520, DuPont). The resistivity of ultrapure water is 18.25 MΩ cm. All chemical reagents can be used without further purification. Furthermore, the nickel foam (NF) in this experiment was purchased from Beijing Join Technology Co., Ltd and cleaned with acetone and diluted hydrochloric acid before use.

2.2. Preparation of electrode materials

2.2.1. Synthesis of FeOOH/NF

To obtain FeOOH through a hydrothermal process, urea (0.964 g, 16 mmol), ammonium fluoride (0.302 g, 8 mmol) and $Fe(NO_3)_3$ 9 H_2O (1.616 g, 2.5 mmol) were added to 60 mL deionized water and stirred for 10 minutes. Subsequently, a piece of nickel foam (3 × 3 cm) was dipped into the solution. The mixture was then transferred to a stainless steel autoclave lined with 100 mL polytetrafluoron. The autoclave was maintained at 120℃ for 12 hours. Afterward, the autoclave was allowed to cool down to room temperature, and the resulting FeOOH/NF was cleaned with ethanol and deionized water multiple times to remove any solid materials adhering to the surface. Finally, the FeOOH/NF was dried in a vacuum at 60℃ for 12 hours.

2.2.2. Synthesis of $NiSe_2$/NF

NaOH (5.8 g, 0.09 mol) and selenium powder (0.36 g, 4 mmol) were added into 60 mL deionized water, and then stirred for 10 minutes, the pre-treated NF (3 × 3 cm^2) was added. Subsequently, the solution and NF were transferred into a stainless steel autoclave lined with 100 mL polytetrafluoron. Which was heated to 180℃ and maintained at that temperature for 8 hours. After cooling to room temperature, the sample was washed with anhydrous ethanol and deionized water multiple times. Finally, it was vacuum dried at 60℃ for 12 h to obtain the $NiSe_2$/NF.

2.2.3. Synthesis of $Fe_2O_3/NiSe_2$-FeOOH/NF

The synthetic steps for $Fe_2O_3/NiSe_2$-FeOOH/NF are the same as $NiSe_2$/NF, in addition to replacing nickel foam with FeOOH/NF.

2.3. Physicochemical characterizations

Prepared materials were characterized by X-ray diffraction (XRD, D8-Focus, BrukerAxs, Germany) in Bragg geometry with Cu Kα radiation at a scanning rate of 5° min^{-1} over a 2θ range of 10–90°. The surface valence states of the samples were checked using X-ray photoelectron spectroscopy (XPS, ESCALAB 250XI, ThermoFisher, USA). The binding energy of C1s originating from carbon pollution was measured at 284.8 eV. Raman spectra were recorded using an Ar ion laser beam (λ = 532 nm) on an RM-1000 instrument in Renishaw, UK, with the source spectrum ranging from 200 to 2500 cm^{-1}. The morphology and microstructure of the samples were studied by scanning electron microscopy (SEM, S-4800, Japan) and transmission electrons microscopy (TEM, Jeol JEM-F200, Japan). Energy dispersion spectroscopy (EDS) was also used to explore the elemental mapping of the prepared sample (INCA Energy 350, OXFORD, England), Inductively Coupled Plasma mass spectrometry (ICP-MS) analysis was undertaken using the Inductively Coupled Plasma Atomic Emission Spectrometer (Agilent 7800). The surface hydrophilicity was measured by JC2000D1 contact angle measuring instrument. X-ray absorption fine structure (XAFS) measurements were conducted on the Table XAFS-500 spectrometer to examine the valence state and coordination of iron species. The XAFS spectra were collected in transmission mode and processed using ATHENA in the Demeter software package. Furthermore, ARTEMIS in the Demeter software package was employed to fit the extended X-ray absorption fine structure (EXAFS) spectra.

2.4. In-situ Raman spectroscopy

Polytetrafluoroethylene electrochemical cells were used to study the combination of electrochemistry and in-situ Raman spectroscopy. In these cells, platinum wire and Hg/HgO electrodes served as the counter and reference electrodes, respectively. Raman measurements were conducted using a Raman spectrometer an Ar ion laser beam (λ = 532 nm) on an RM-1000 instrument in Renishaw, UK, equipped with a 50x objective and each in-situ spectrum covered a wavelength range of

200–1400 cm^{-1}. To ensure the reliability of the obtained spectra, the Raman displacement was calibrated using monocrystalline silicon (520.7 cm^{-1}). The exposure time for each spectrum was 3 seconds, with 10 accumulated scans. A CHI 660E was used to continuously apply potential during the acquisition of Raman spectra.

2.5. Electrochemical measurement

All electrochemical measurements were conducted using a three-electrode standard system at the electrochemical workstation (CHI 660E) unless otherwise specified. The prepared sample (1 × 1.5 cm) served as the working electrode (WE), while Hg/HgO and a graphite rod with a diameter of 4 mm were used as the reference electrode and the counter electrode, respectively. Prior to the experiments, all electrochemical cell components were cleaned with 1 M H$_2$SO$_4$ and rinsed with copious amounts of 18.2 MΩ·cm H$_2$O. All working electrodes were electrochemically preactivated by several cyclic voltammetric (CV) scans at a scan rate of 10 mV s^{-1} until it is stable. The tests were performed in 1.0 M KOH aqueous solution and the linear sweep voltammetry (LSV) test for OER was carried out at a scan rate of 5 mV s^{-1}. Electrochemical impedance spectroscopy (EIS) was performed in the frequency range of 100,000 to 0.1 Hz with an amplitude of 50 mV. The electrochemical surface area (ECSA) of the catalyst was estimated using cyclic voltammetry to measure the double-layer capacitance (C_{dl}) at different scanning rates in the non-faraday process region, according to the equation:

$$ECSA = \frac{C_{d1}}{C_s} \tag{1}$$

Where C_{dl} is determined by plotting Δj (ja-jc) at different scan rates, and specific capacitance (2.5 mF cm^{-2}), respectively [25]. In addition, potentials were converted to a reversible hydrogen electrode (V vs RHE) using Nernst's equation:

$$E_{RHE} = E_{Hg/HgO} + 0.0591 \times pH + 0.098 \tag{2}$$

The stability of the samples was assessed by chronopotentiometry (CP) curve at a constant current density of 10 mA cm^{-2}. All potentials in this study were corrected using iR compensation (90%). The electrochemical tests were conducted at room temperature (25℃).

2.6. Theoretical calculations

DFT calculations were carried out using the VASP code. For exchange-correlation, the Perdew-Burke-Ernzerhof (PBE) functional within the generalized gradient approximation (GGA) was employed. The expansion of the electronic eigenfunctions was described using the projector-augmented-wave pseudopotential (PAW) with a kinetic energy cut-off of 500 eV. To minimize interlayer interactions, a vacuum thickness of 25 Å was set. A Brillouin-zone integration was performed using a Γ-centered 5 × 5 × 1 Monkhorst-Pack k-point. Full relaxation of atomic positions was done until the energy and force reached a tolerance of 1 × 10^{-5} eV and 0.03 eV/Å, respectively. The dispersion-corrected DFT-D method was employed to account for long-range interactions. The Gibbs free energy change (ΔG) was calculated using the computational hydrogen electrode (CHE) model, according to Eq. (1):

$$\Delta G = \Delta E + \Delta ZPE - T\Delta S \tag{3}$$

Here, ΔE represents the reaction energy obtained by the total energy difference between the reactant and product molecules absorbed on the catalyst surface, ΔS indicates the change in entropy for each reaction, and ΔZPE is the zero-point energy correction to the Gibbs free energy. The T represents room temperature, which was set at 298.15 K.

3. Results and discussion

3.1. Material structure characterizations

FeOOH nanosheets were first synthesized on nickel foam using a typical method, as shown in Fig. 1a. The morphology of FeOOH nanosheets can be seen in Figure S1. FeOOH undergoes slow dehydration to Fe$_2$O$_3$ at 180°C. Nickel foam slowly releases Ni^{2+} in an alkaline environment and is converted to NiSe$_2$ by selenization and the detailed reaction mechanism can be found in Table S1. The formation of heterostructures is analogous to the Ostwald ripening effect, with the loading amount of heterostructures increasing with selenization time. This is supported by Figure S2. which demonstrates that both the size and number of heterojunction nanoparticles gradually increase with longer reaction times. The surface components of the Fe$_2$O$_3$/NiSe$_2$-FeOOH/NF are gently scraped for X-ray diffraction (XRD), thus reducing the interference of the peak strength of the nickel foam. To investigate the crystalline structures, the XRD patterns of as-prepared samples were demonstrated. From Figure S3a, the peaks related to NiSe$_2$ (JCPDS No: 88–1711) can be observed at 29.9° (200), 33.5° (210), 36.9° (211), 42.8° (220), 50.7° (311), 55.5° (023), 57.8° (321), 72.6° (421), 84.3° (511), 88.1° (234) (orange diamond marks), indicating the successful synthesis of highly crystalline NiSe$_2$ while the diffraction peaks centered at 24.1°, 33.1°, 35.6°, 40.8°, 49.4°, 54.0°, 62.3° and 63.9° planes (blue heart marks) matched well with the (012), (104), (110), (113), (024), (116), (214) and (300) crystal planes of Fe$_2$O$_3$ (JCPDS No. 72–0469). Peaks at 33.1° and 33.5° are observed to be very close and relatively sharp, attributing to Fe$_2$O$_3$ and NiSe$_2$, respectively. This indicates that they have similar interplanar spacing. Generally, similar interplanar spacing facilitates mutual alignment at the interface, reducing lattice mismatch-induced distortions and promoting the formation of heterojunctions. Only a weak peak belonging to FeOOH (110) was observed at 11.8° (gray square marks) which may be attributed to FeOOH acting as source of Fe$_2$O$_3$, resulting in a decrease in crystallinity. Moreover, the intensity of these peaks is relatively weak, indicating the formation of only small-sized nanoparticles. In conclusion, we have successfully synthesized multi-phase heterogeneous structures. Furthermore, Figure S3b and S3c present the XRD patterns of NiSe$_2$/NF and FeOOH/NF respectively, with their observed peaks matching well with NiSe$_2$ (JCPDS No. 88–1711) and FeOOH (JCPDS No. 01–0662), except for the inevitable intense Ni (JCPDS No. 87–0712) peaks. It is important to mention that all samples are impurity-free, suggesting high phase purity in the samples. The scanning electron microscopy (SEM) images of Fe$_2$O$_3$/NiSe$_2$-FeOOH/NF reveal its three-dimensional structure (Fig. 1b), in which FeOOH maintains an interlocked sheet structure with a few holes on the surface. Additionally, spherical particles with a diameter of about 300 nm are vertically loaded on the porous FeOOH (Fig. 1c and S4). The high hydroxyl surface enhances hydrophilicity and promotes mass transfer by increasing the concentration of reactants. The high-resolution transmission electron microscopy (HRTEM) of Fe$_2$O$_3$/NiSe$_2$-FeOOH/NF was further characterized by ultrasonic dispersion. As shown in Fig. 1d, nanocrystals of different sizes are tightly bound at the atomic level. These nanocrystallites exhibit visible lattice fringes with interplanar spacing of 0.20 and 0.24 nm, corresponding to the (110) and (202) of Fe$_2$O$_3$ (yellow font), respectively. Furthermore, the interplanar spacing of 0.25 and 0.29 nm, corresponding to the (221) and (222) of NiSe$_2$ (white font), can also be identified (More specific details are shown in Figure S5).

High-angle toroidal dark-field scanning transmission electron microscopy (HAADF-STEM) demonstrates the uniformity of the entire particle without the presence of a precipitated phase (Fig. 1e). The fast Fourier transform (FFT) images indicate clear spots (Figs. 1f, 1g), suggesting that these nanocrystals are single crystals and the clear interfaces confirm the formation of heterojunctions. Energy dispersive X-ray spectroscopy (EDS) confirms the strong uniform distribution of Fe$_2$O$_3$ and NiSe$_2$, which is consistent with the observation from HAADF-STEM.
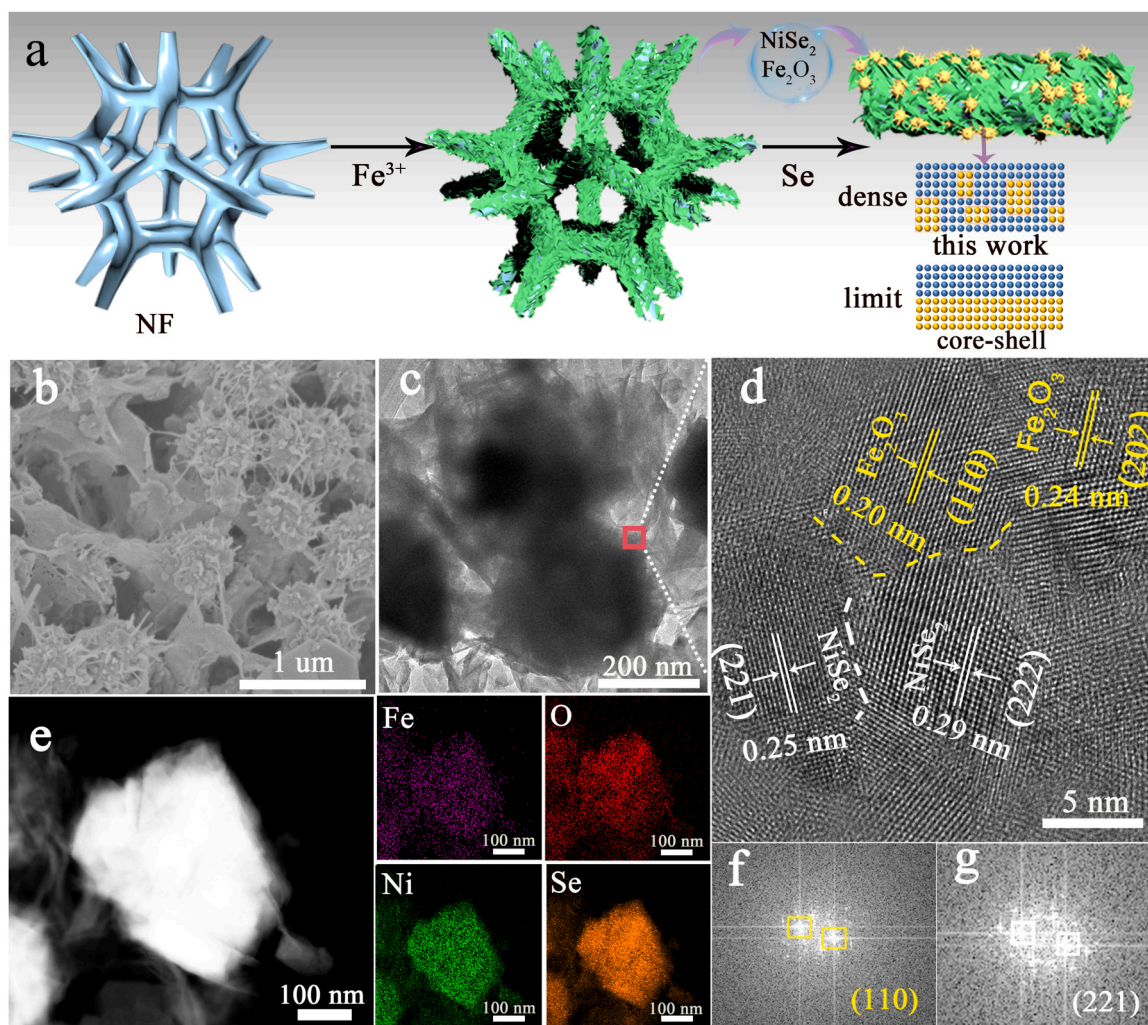
Fig. 1. (a) Schematic illustration of fabricating $Fe_2O_3/NiSe_2$ on NF. (b) SEM image (c) TEM and (d) HRTEM images of $Fe_2O_3/NiSe_2$-FeOOH/NF. (e) HAADF-STEM images and the corresponding elemental mappings(Fe,O,Ni,Se). (f) and (g) represent FFT diffraction pattern of HRTEM images (Fig. 1d).

Furthermore, a more detailed crystal distribution analysis can be found in the Figure S6, it manifests a crowded arrangement of significant quantity lattice fringes with clear interfaces. Interplanar spacing which is Fourier transformed by lattice fringes exhibit a well congruence with XRD data and the corresponding Miller Indices have been meticulously documented in Table S2. In conclusion, based on the comprehensive characterizations presented above, a robust demonstration can be made to establish $Fe_2O_3/NiSe_2$-FeOOH/NF as a heterojunction characterized by a dense interface.

The valence states and chemical bonding configurations of the fabricated catalysts were meticulously analyzed through X-ray photoelectron spectroscopy (XPS) and Raman spectroscopy, providing crucial insights into their electronic structures. The high-resolution XPS survey spectra (Figure S7) reveal the presence of additional Fe peak along with Ni, Se, and O elements in $Fe_2O_3/NiSe_2$-FeOOH/NF in contrast to $NiSe_2$/NF. Specifically, the minor peaks at 855.2 and 873.8 eV can be attributed to Ni $2p_{3/2}$ and Ni $2p_{1/2}$ peaks of Ni^{3+} arising from the inevitable oxidation on the surface of $NiSe_2$ (Fig. 2a), the peaks located at 853.5 and 870.8 eV correspond to Ni $2p_{3/2}$ and Ni $2p_{1/2}$ peaks in $NiSe_2$ [26, 27]. In addition, the wide peaks at 861.4 and 879.5 eV are typical satellite peaks of Ni $2p_{3/2}$ and Ni $2p_{1/2}$, the binding energy of $Fe_2O_3/NiSe_2$-FeOOH/NF peaks moves about 0.2 eV in the direction of higher binding energy compared with $NiSe_2$/NF, which may be due to the strong interfacial electron interaction. Notably, the proportion of Ni^{3+} in the Ni 2p peak area increased from 15.1% of $NiSe_2$/NF to 25.9%. As for

the Fe 2p spectrum (Fig. 2b), $Fe_2O_3/NiSe_2$-FeOOH/NF contains two asymmetrical main peaks belonging to Fe $2p_{3/2}$ at 712.2 eV and Fe $2p_{1/2}$ at 724.7 eV, which can be further divided into two sub-peaks Fe^{3+} ($2p_{3/2}$ about 713.8 eV, $2p_{1/2}$ about 725.7 eV) and Fe^{2+} ($2p_{3/2}$ about 711.0 eV, $2p_{1/2}$ about 723.1 eV) [28]. A satellite peak can be detected at 718.2 eV, and all $Fe_2O_3/NiSe_2$-FeOOH/NF binding energy peaks shift 0.2 eV toward lower binding energy relative to the Fe_2O_3. Contrary to the change in Ni^{3+}, the proportion of Fe^{2+} in Fe 2p of heterojunctions increases to 44.4%, while in Fe_2O_3, the proportion of Fe^{2+} in Fe 2p is 27%. This implies that the average oxidation state of Fe decreases during the formation of heterojunctions, indicating that electron transfer occurs at the position where Fe acts as the acceptor. Ni serves as the electron donor, and electrons are explicitly transferred to Fe. The Se 3d spectrum (Fig. 2c) could be fitted into two peaks of 54.52 eV (related to Se $3d_{5/2}$) and 55.49 eV (related to Se $3d_{3/2}$) [17,18]. In addition, the peak at 59.06 eV is from SeO_x, attributed to the surface oxidation. It is worth mentioning that Se 3d also exhibits a high binding energy shift of 0.2 eV, which implies that the oxidation state becomes higher than $NiSe_2$/NF due to the strong coupling effect of Fe^{3+} and Ni^{2+}. Concerning oxygen in the catalyst samples, XPS spectra in Fig. 2d could be deconvoluted into three peaks. The peaks centers at 530.3, 531.6 and 532.8 eV are respectively attributed to M-O, M-OH and absorbed oxygen [29]. It is important to note that the content of -OH on the surface of FeOOH reaches 80.4%, significantly higher than that of $NiSe_2$ (21.1%). Meanwhile, the chemical bonds in the catalyst were further characterized by
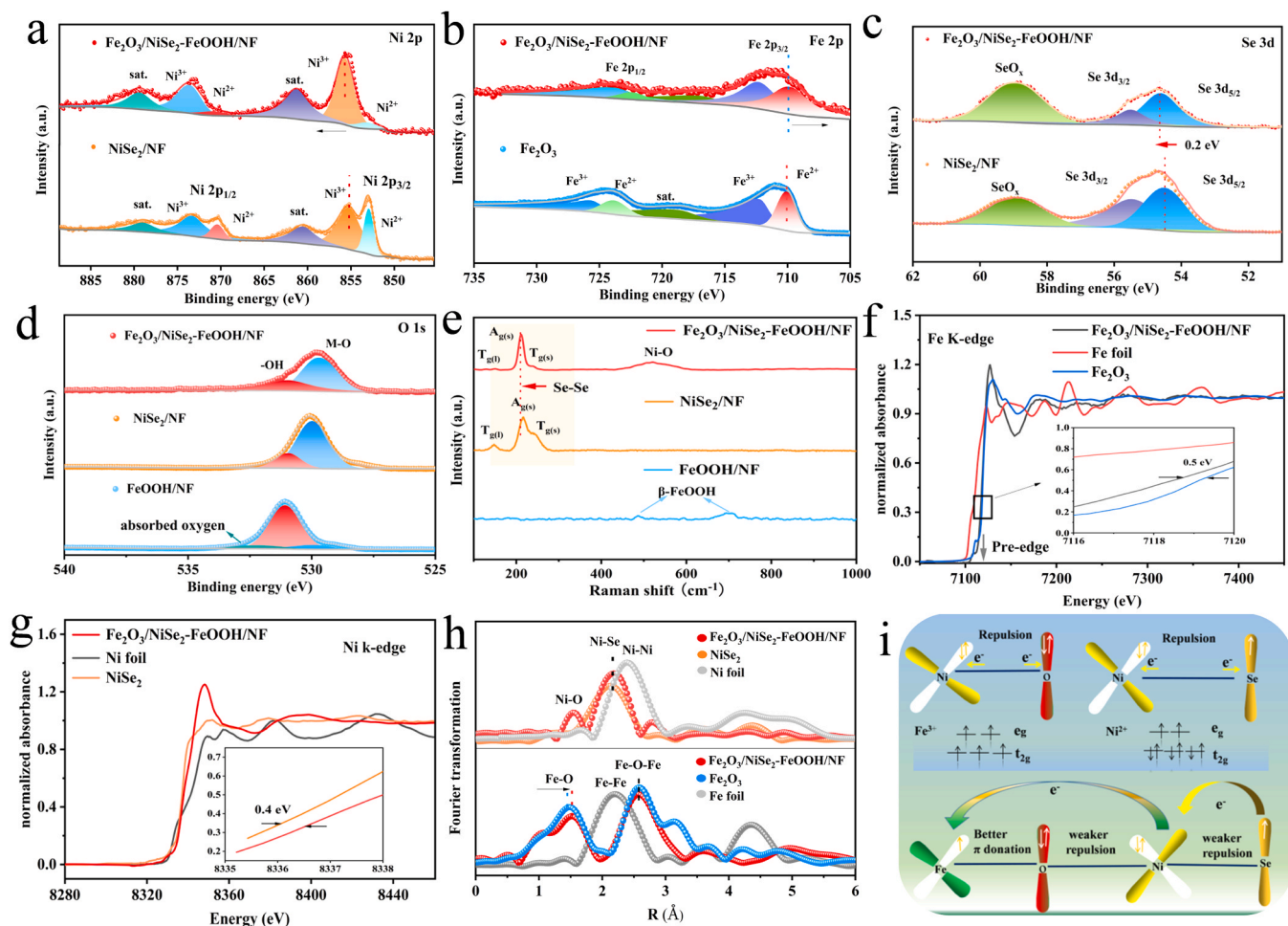
Fig. 2. (a) Ni 2p, (b) Fe 2p, (c) Se 3d of Fe$_2$O$_3$/NiSe$_2$-FeOOH/NF, Fe$_2$O$_3$ and NiSe$_2$/NF. (d) O 1 s spectra of Fe$_2$O$_3$/NiSe$_2$-FeOOH/NF, FeOOH/NF and NiSe$_2$/NF. (e) Raman spectra. (f) Normalized XANES spectra near Fe K-edges of Fe$_2$O$_3$/NiSe$_2$-FeOOH/NF, commercial Fe$_2$O$_3$ samples and Fe foil. (g) Normalized XANES spectra near Ni K-edges of Fe$_2$O$_3$/NiSe$_2$-FeOOH/NF, commercial NiSe$_2$ samples and Ni foil. (h) Fourier transformations of k^3-weighted EXAFS spectra. (i) Schematic diagram of valence electron coupling.

Raman spectroscopy, as shown in Fig. 2e. The as-prepared NiSe$_2$ shows characteristic peaks at 155, 216, and 243 cm^{-1} for Tg (libration), Ag (stretching), and Tg (stretching) modes, respectively [30]. The peak at 216 cm^{-1} is red shifted by 5 cm^{-1} relative to NiSe$_2$/NF, which may be due to the interaction of Ni-O. The peak around 524 cm^{-1} is attributed to the Ni-O-Fe bonds of Fe$_2$O$_3$/NiSe$_2$-FeOOH/NF. Besides, there are two peaks at 487 and 710 cm^{-1} that appeared in the FeOOH/NF, which can be attributed to the β-FeOOH phase [31,32].

To obtain a more precise understanding of the fine electronic structure and local coordination environment of Fe$_2$O$_3$/NiSe$_2$-FeOOH/NF, we conducted X-ray absorption spectroscopy (XAS) analysis at both the Fe K-edge and Ni K-edge. Fig. 2f demonstrates that the absorption edge of the X-ray absorption near-edge structure (XANES) spectrum for Fe closely resembles that of the reference material Fe$_2$O$_3$, suggesting that the oxidation state of Fe is slightly lower than Fe^{3+} within Fe$_2$O$_3$/NiSe$_2$-FeOOH/NF. The reduction in Fe$_2$O$_3$/NiSe$_2$-FeOOH/NF relative to the edge peak of Fe$_2$O$_3$ further suggests a decrease in the symmetry of Fe within Fe$_2$O$_3$/NiSe$_2$-FeOOH/NF. This symmetry reduction may be attributed to strong coupling effects between Fe and Ni. Furthermore, the XANES spectrum (Fig. 2g) of Ni within Fe$_2$O$_3$/NiSe$_2$-FeOOH/NF exhibits a higher oxidation state compared to Ni^{2+}, which aligns with XPS results. Moving on to Fourier-transform extended X-ray absorption fine structure (EXAFS) spectra, they offer additional insights into the local structure (Fig. 2h). These spectra confirm the presence of Ni-Se scattering paths at approximately 2.18 Å, consistent with those found

in commercial NiSe$_2$. Additionally, we note a subtle Ni-O bond at 1.51 Å [33] in the first shell of Fe$_2$O$_3$/NiSe$_2$-FeOOH/NF but not in NiSe$_2$. This observation suggests potential Ni-O bonding at the interface which is consistent with the Raman spectrum. Simultaneously, identifying Fe-O bonds and Fe-O-Fe [34] in both the first and second coordination shells, in agreement with the results for commercial Fe$_2$O$_3$, serves as proof of the existence of Fe$_2$O$_3$. In-depth analysis was further conducted through fit on the EXAFS data (Figure S8, Table S3 and S4). In comparison to the theoretical coordination number of 6 for NiSe$_2$, the coordination number of Ni-Se within Fe$_2$O$_3$/NiSe$_2$-FeOOH/NF was determined to be 4.8. This indicates that the dense heterogeneous interface results in a significant involvement of unsaturated Ni coordination in bonding with O. It can be observed from the above discussion that oxygen exists at the heterojunction in a bridging manner, and its electron transfer mechanism can be elucidated based on the electron configuration depicted in Fig. 2i. The interaction between Ni^{2+} (t$_{2\,g}^6$e$_g^2$) and Ni^{3+} (t$_{2\,g}^6$e$_g^1$) with O^{2-} and Se$_2^{2-}$ is hindered due to the e$^-$-e$^-$ repulsion, as they possess fully occupied π-symmetric (t$_{2\,g}$) orbitals without any unpaired electrons, thereby obstructing charge transfer. Conversely, Fe^{3+} (t$_{2\,g}^3$e$_g^2$), which is in a high spin state, has three unpaired electron bridges in its corresponding π-symmetric (t$_{2\,g}$) orbital. The primary interaction of Fe^{3+} with O^{2-} is through π donation. Upon the coupling of Ni^{2+} and Fe^{3+}, the π-donating energy of Fe-O becomes stronger due to the e$^-$-e$^-$ repulsion of Ni-O, which will induce a partial electron transfer from Ni to Fe. Meanwhile, the Se−Se bonds are covalent with pairwise

pσ and pπ bonding for $NiSe_2$, the electron filling degree of the eg band is reduced due to the strong coupling effect of Fe^{3+} and Ni^{2+}, we expect the covalent bond in the Se_2^{2-} dimer to be disrupted, leading to the transfer of some charge from the Se-p orbital to the Ni-e_g orbital, form a unique oxidation state of $Ni^{2+\sigma}$ ($t_{2g}^6 e_g^{1+\sigma}$), thus reducing the electron repulsion between $Ni^{2+\sigma}$ and Se_2^{2-} [19,35], the oxidation state of Se is enhanced which is consistent with the XPS results. Significantly, $t_{2g}^6 e_g^{1+\sigma}$ tends towards the favorable $e_g^{1.2}$ electronic configuration, enabling the establishment of σ-bonds with adsorbed oxygen in the course of the OER [36,37]. Hence, the distinctive Se-Ni-O-Fe bonding configuration fine-tunes the electronic state of Ni. Moreover, the advantageous dual-modification from both Fe and Se results in a moderate oxidation state of Ni heightens the binding energy with oxygen-containing intermediates, consequently enhancing the catalytic activity of the OER and expediting the rate of the reaction.

3.2. Oxygen evolution performance

Detailed electrochemical measurements were performed in O_2-saturated 1 M KOH to evaluate the electrocatalytic performance towards OER. According to the linear sweep voltammetry (LSV) curves with iR compensation (Fig. 3a), the activity order of the catalysts is Fe_2O_3/$NiSe_2$-FeOOH/NF> $NiSe_2$/NF> FeOOH/NF. Specifically, Fe_2O_3/$NiSe_2$-FeOOH/NF exhibits remarkable catalytic activity, with a small overpotential of 169 mV at 10 mA cm^{-2} and 230 mV at 100 mA cm^{-2}, significantly lower than $NiSe_2$/NF (181 mV at 10 mA cm^{-2}, 470 mV at 100 mA cm^{-2}) and FeOOH/NF (240 mV at 10 mA cm^{-2}, 450 mV at 100 mA cm^{-2}), surpassing most reported catalysts in alkaline electrolytes (Fig. 3b). $NiSe_2$/NF displays an oxidation peak at approximately 1.4 V attributed to Ni^{2+} to Ni^{3+}. The polarization curve analysis further reveals that Fe_2O_3/$NiSe_2$-FeOOH/NF has a Tafel slope of 31.2 mV dec^{-1} (Fig. 3c), indicating faster reaction kinetics of OER. Moreover, its reaction kinetics are superior to most of currently reported highly active OER catalysts (Table S5). To investigate the kinetics further, electrochemical impedance spectroscopy (EIS) measurements were performed in a 1.0 M KOH solution. A Nyquist diagram based on the equivalent circuit can be seen in Fig. 3d. It is evident that all of the tested materials exhibit a semicircular shape. The diameter of this semicircle corresponds to the charge transfer resistance (R_{ct}). A smaller R_{ct} indicates a stronger charge transfer ability. Fig. 3b demonstrates that Fe_2O_3/$NiSe_2$-FeOOH/NF has a lower R_{ct} of 0.8 Ω, indicating a stronger charge transfer ability compared to $NiSe_2$/NF (1.0 Ω) and FeOOH/NF (1.5 Ω). The enhanced charge
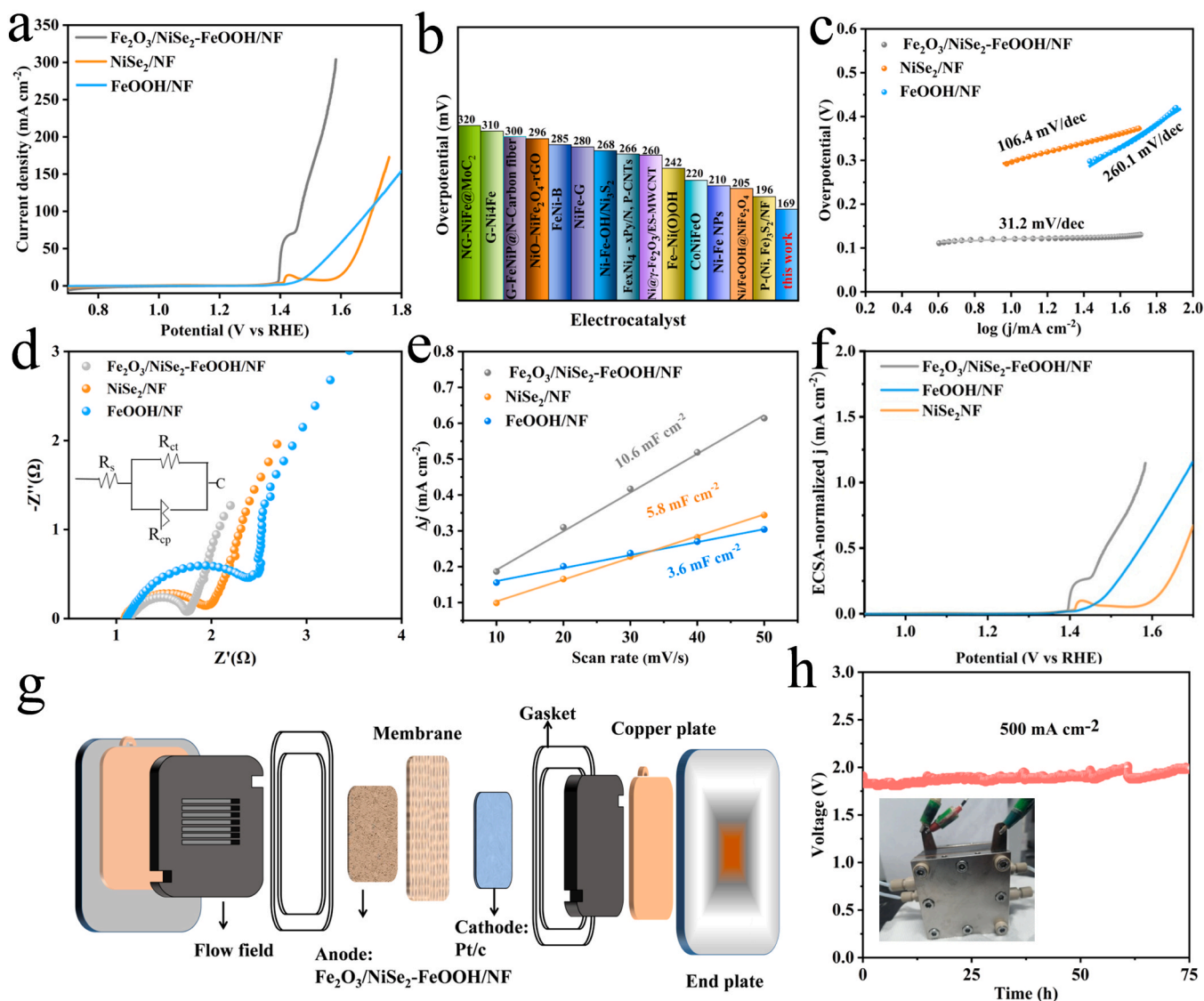
Fig. 3. (a) LSV curves at a scan rate of 5 mV s^{-1} in 1 mol L^{-1} KOH. (b) Comparison of overpotential at a current densitiy of 10 mA cm^{-2} for the prepared catalysts. (c) Tafel plots, (d) Nyquist plots, (e) C_{dl} curves and (f) ECSA-normalized LSV curves of Fe_2O_3/$NiSe_2$-FeOOH/NF, FeOOH/NF and $NiSe_2$/NF, (g) Schematic illustration of the AEM electrolyzer, (h) Durability test of the AEM electrolyzer catalyzed at 0.5 A cm^{-2} for 75 h.

transfer capability of Fe_2O_3/$NiSe_2$-FeOOH/NF is attributed to the high interface density, which optimizes electron distribution and modifies the band structure. Evaluating the ECSA from double-layer capacitance (C_{dl}) in the non-Faradic potential region, Figure S9 illustrates CV curves obtained at varying scanning rates. From Fig. 3e, it is evident that Fe_2O_3/$NiSe_2$-FeOOH/NF possesses a higher C_{dl} value (10.6 mF cm^{-2}) significantly greater than $NiSe_2$/NF (5.8 mF cm^{-2}) and Fe_2O_3/NF (3.6 mF cm^{-2}), which is due to its porous three-dimensional structure. To further assess the intrinsic activity of the catalyst, ECSA normalization was performed across all materials, normalizing LSV curves by ECSA (Fig. 3f) demonstrates that the intrinsic OER activity of Fe_2O_3/$NiSe_2$-FeOOH/NF is significantly superior to $NiSe_2$/NF and FeOOH/NF, suggesting that the improved electrochemical performance arises from the optimized intrinsic activity rather than differences in ECSA.

Furthermore, the contact angle is widely recognized as a sensitive indicator of interface ion/molecular interactions and alterations. Therefore, we conducted static contact angle measurements to assess the surface wettability of the materials. Figure S10 becomes evident that both FeOOH/NF and Fe_2O_3/$NiSe_2$-FeOOH/NF exhibit negligible contact angles, in contrast, the contact angle of $NiSe_2$ measures at 17.14°, demonstrating that FeOOH combines with the heterojunction to create a superhydrophilic surface. Consequently, this promotes the adsorption kinetics of surface substances effectively [38]. The OER performance of the catalysts under different selenization times was investigated, as shown in Figure S11. Apparently, the catalyst selenized for 8 hours exhibited the best OER performance. Therefore, this sample was selected as the main focus of this study. The Fe_2O_3/$NiSe_2$-FeOOH/NF electrode underwent a long-term durability test using chronopotentiometry (CP) at a constant current density of 10 mA cm^{-2} for 200 hours (Figure S12). Remarkably, the electrode displayed excellent oxygen evolution output without any noticeable degradation. Subsequently, the electrodes were subjected to characterization using XPS and SEM, which confirmed that the morphology remained similar to that of the initial material. XPS results (Figure S13) of the initial and post-stability catalysts revealed that all characteristic peaks were still detectable after the OER stability test, and the relative intensity of Ni^{3+} and SeO_x increased, suggesting significant surface oxidation of catalyst due to the prolonged OER process. SEM image (Figure S14) also showed consistent nanoparticle loading on the interlocked nanosheets, with the only noticeable difference being trace dissolution of the nanowires located on the nanoparticle. This dissolution was attributed to the precipitation of Se resulting from the incorporation of oxygen, consistent with previous studies [39]. Additionally, we further measured the concentration of dissolved selenium ions in electrolyte at 10 mA cm^{-2} for 200 h by ICP-MS and the results are summarized in Table S6, which reveals a higher selenium ions content (4.15×10^{-3}%) in the electrolyte of $NiSe_2$/NF compared to Fe_2O_3/$NiSe_2$-FeOOH/NF (4.86×10^{-4}%), indicating that the dense heterojunction had a positive effect in stabilizing Se. To evaluate the practical applicability of the prepared OER electrocatalyst in a water electrolysis system, an anion exchange membrane (AEM) cell was assembled, and detailed process information and AEM configuration are provided in the appendix (Figure S15). In the AEM, Fe_2O_3/$NiSe_2$-FeOOH/NF serves as the anode for OER, as illustrated in Fig. 3g. Pt/C, recognized as the best HER electrocatalyst, is employed as the cathode to minimize polarization losses induced by HER. Specifically, the assembled AEM electrolysis cell requires only 1.8 V at a current of 0.5 A cm^{-2}, and after stable operation for 75 hours (Fig. 3h), only a slight performance decay (6.2%) is observed in the electrolysis cell's performance. Based on these comprehensive characterization results, it can be strongly concluded that the Fe_2O_3/$NiSe_2$-FeOOH/NF electrocatalyst demonstrated remarkable stability and efficiency for OER.

3.3. Electrocatalytic performance in seawater electrolytes

Given the outstanding catalytic performance of the Fe_2O_3/$NiSe_2$-

FeOOH/NF, we obtained natural seawater from the Bohai Sea area of China (Figure S16) and prepared alkaline natural seawater (1 M KOH + seawater) to investigate the OER performance in alkaline natural seawater electrolyte, as shown in Fig. 4a, Fe_2O_3/$NiSe_2$-FeOOH/NF exhibited superior OER performance compared to the currently reported catalyst (Table S7). To avoid the influence of oxidation peaks on overpotential, we selected the overpotential at a current density of 200 mA cm^{-2}, and its performance still exceeds that of many reported catalysts (Table S8). Morever, at a typical current density of 400 mA cm^{-2}, Fe_2O_3/$NiSe_2$-FeOOH/NF only required an overpotential of 370 mV, which is significantly lower than the 490 mV overpotential required for the oxidation of chloride to hypochlorite. It is worth mentioning that Fe_2O_3/$NiSe_2$-FeOOH/NF also demonstrated superior HER performance (Fig. 4b), with overpotentials of only 134 mV and 233 mV at 10 mA cm^{-2} and 100 mA cm^{-2}, respectively, significantly lower than those of FeOOH/NF (η_{10} = 196 mV, η_{100} = 376 mV) and $NiSe_2$/NF (η_{10}= 176 mV, η_{100} = 395 mV). We conducted further research on the overall seawater electrolysis performance of both catalysts by integrating them into a dual-electrode alkaline electrolysis cell. In this setup, Fe_2O_3/$NiSe_2$-FeOOH/NF served as the anode for OER and the cathode for HER (Fig. 4d). We collected the gas products generated at the cathode and anode of the H-type cell in 1 M KOH + seawater electrolyte to evaluate the Faradaic efficiency (Figure S17). As shown in Fig. 4c, the volume ratio of H_2 and O_2 released at the cathode and anode is close to 2:1 (theoretical value), demonstrating a high level of selectivity for OER. A 0.5 M KI reagent solution was employed to detect ClO^- collected in the solution after the anodic reaction using iodometric titration, as described by chemical reactions (4−6):

$$KI \rightarrow K^+ + I^- \tag{4}$$

$$ClO^- + 2I^- + H_2O \rightarrow Cl^- + I_2 + 2OH^- \tag{5}$$

$$I_2 + I^- \rightarrow I_3^- \tag{6}$$
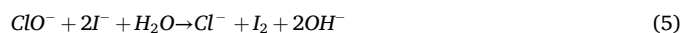
I_3 can be measured by UV–visible absorption spectroscopy. As a comparison, we performed stable electrolysis for 60 minutes at 50 mA cm^{-2} using 0.01 M KOH + seawater and 1 M KOH + seawater, respectively. As depicted in Figure S18, a prominent absorption peak occurs at 352 nm in the 0.01 M KOH + seawater electrolyte. This observation suggests the presence of the byproduct ClO^-, which can be attributed to the substantial overpotential required to facilitate the competitive chlorine evolution reaction (CER) at 50 mA cm^{-2} under weak alkaline conditions. In contrast, no I_3^- was detected in the 1 M KOH + seawater, indicating close to 100% efficiency in OER in a strongly alkaline environment, consistent with the findings presented in Fig. 4c. Notably, during continuous testing over 100 hours at 100 mA cm^{-2} in the 1 M KOH + seawater, there was only a slight increase in potential fluctuations (Fig. 4d), underscoring the substantial potential for practical hydrogen production from natural seawater.

3.4. Mechanism analysis

Theoretical calculation is carried out to further unveil the internal reasons for the improvement of heterojunction OER performance. Fe_2O_3 (110) and $NiSe_2$ (221) planes were selected as DFT simulation models and the optimized heterojunction model of Fe_2O_3/$NiSe_2$ is shown in Fig. 5a, the utilization of thin layers is employed to explore interface electron effects and interactions. Electron density difference analysis reveals the occurrence of charge density difference at the heterojunction interface (Fig. 5b), with the yellow representing accumulation and the blue representing consumption. Given the lower electronegativity of Se (2.55) compared to O (3.44), the electron accumulation and depletion around Ni atoms can be ascribed to the electron transfer from Se to Ni and the electron attraction by O, respectively, while electron accumulation is observed around Fe, which is consistent with the XPS analysis.

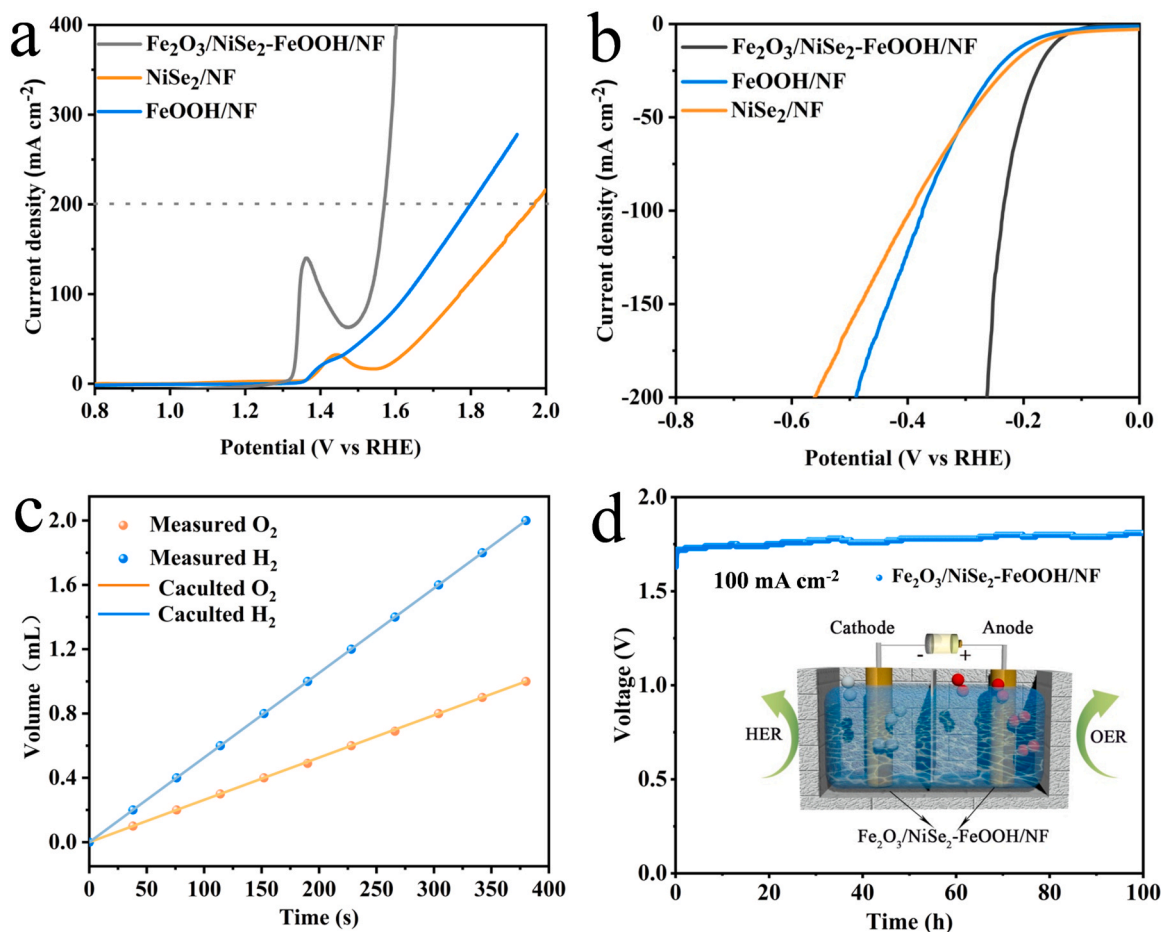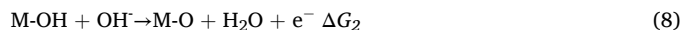Density of states (DOS) was conducted to reveal the intrinsic

Fig. 4. (a) OER and (b) HER polarization curves in 1 M KOH + seawater. (c) Collected H_2 and O_2 volume images generated of water-splitting. (d) Durability test of $Fe_2O_3/NiSe_2$-FeOOH/NF catalyzed dual-electrode electrolysis cell under 0.1 A cm^{-2}.

advantage of superior performance. As shown in Fig. 5(d-f), all samples can cross the Fermi level, highlighting their well electrical conductivity. The increase in the total density of states of $Fe_2O_3/NiSe_2$ near the Fermi level indicates its rapid electron transfer ability. The projected density of states (PDOS) shows that the d-band center (ε_d) of $NiSe_2$ and Fe_2O_3 are -3.34 eV and -1.87 eV, respectively. According to the optimized $Fe_2O_3/NiSe_2$ heterojunction, ε_d-Fe and ε_d-Ni are -2.08 and -1.78 eV, respectively. The d-band center theory is commonly employed to explain the strength of interaction between adsorbents and surfaces, as the energy level of the d-band center influences the filling of the anti-bond band and ultimately determines the stability and strength of adsorption bond formation. An excellent catalyst should have a moderated d-band center to ensure balanced binding strength between the adsorption and the active site. Too strong binding strength between the active site and the intermediate can result in surface poisoning, hindering oxygen desorption. Conversely, if the binding energy is too weak, it will restrict the utilization of the intermediate. The results convincingly indicate that the d-band center of ε_d-Fe and ε_d-Ni in $Fe_2O_3/NiSe_2$ is moderate when contrasted with $NiSe_2$ and Fe_2O_3, which implies that the enhancement of interfacial charge transfer positively influences the d-band center within the heterojunction, leading to effective adsorption of oxygen-containing intermediates and oxygen desorption. Additionally, the optimal free energy change of intermediates and products catalyzed by electrocatalysts was calculated (Fig. 5c). In alkaline media, OER is generally considered to be the following process [39]:

$$M + OH^- \rightarrow M\text{-}OH + e^- \quad \Delta G_1 \tag{7}$$

$$M\text{-}OH + OH^- \rightarrow M\text{-}O + H_2O + e^- \quad \Delta G_2 \tag{8}$$

$$M\text{-}O + OH^- \rightarrow M\text{-}OOH + e^- \quad \Delta G_3 \tag{9}$$

$$M\text{-}OOH + OH^- \rightarrow M\text{-}O_2 + H_2O + e^- \quad \Delta G_4 \tag{10}$$

Where M refers to the catalyst. Various intermediates such as M-OH, M-O, M-OOH, and M-O_2 are formed. In the $Fe_2O_3/NiSe_2$ model, Fe and Ni serve as the active sites respectively, the adsorption configurations of Fe and Ni in $Fe_2O_3/NiSe_2$-FeOOH/NF is shown in Table S9 and Table S10. Fig. 5c vividly demonstrates all the three catalysts display uphill pathway for OER catalysis. Hence, the step characterized by the most significant change in free energy represents the rate-determining step (ΔG_{rds}) in the process of OER. The outcomes unequivocally establish that the formation of *OOH represents the ΔG_{rds}, and the maximum free energies of the Fe and Ni sites of the $Fe_2O_3/NiSe_2$ heterojunction are $\Delta G_{rds} = 1.76$ and 1.63 eV, respectively. While Fe_2O_3/NF ($\Delta G_{rds} = 1.80$ eV) and $NiSe_2$/NF ($\Delta G_{rds} = 1.89$ eV), ΔG_{rds} verifies that interfacial charge transfer effectively reduces the barrier formed by *OOH in $Fe_2O_3/NiSe_2$, further optimizing the intermediate formation step of OER. Broadly speaking, owing to the robust electronic rearrangement effect at the interface, the heterostructure manifests exceptional electronic conductivity coupled with apt intermediary adsorption characteristics. As a result, $Fe_2O_3/NiSe_2$-FeOOH/NF showcases heightened performance in OER.

3.5. In-situ Raman spectroscopy analyses

More in-depth structural characterizations of the catalysts were performed through in-situ Raman measurements (Figure S19) to gain
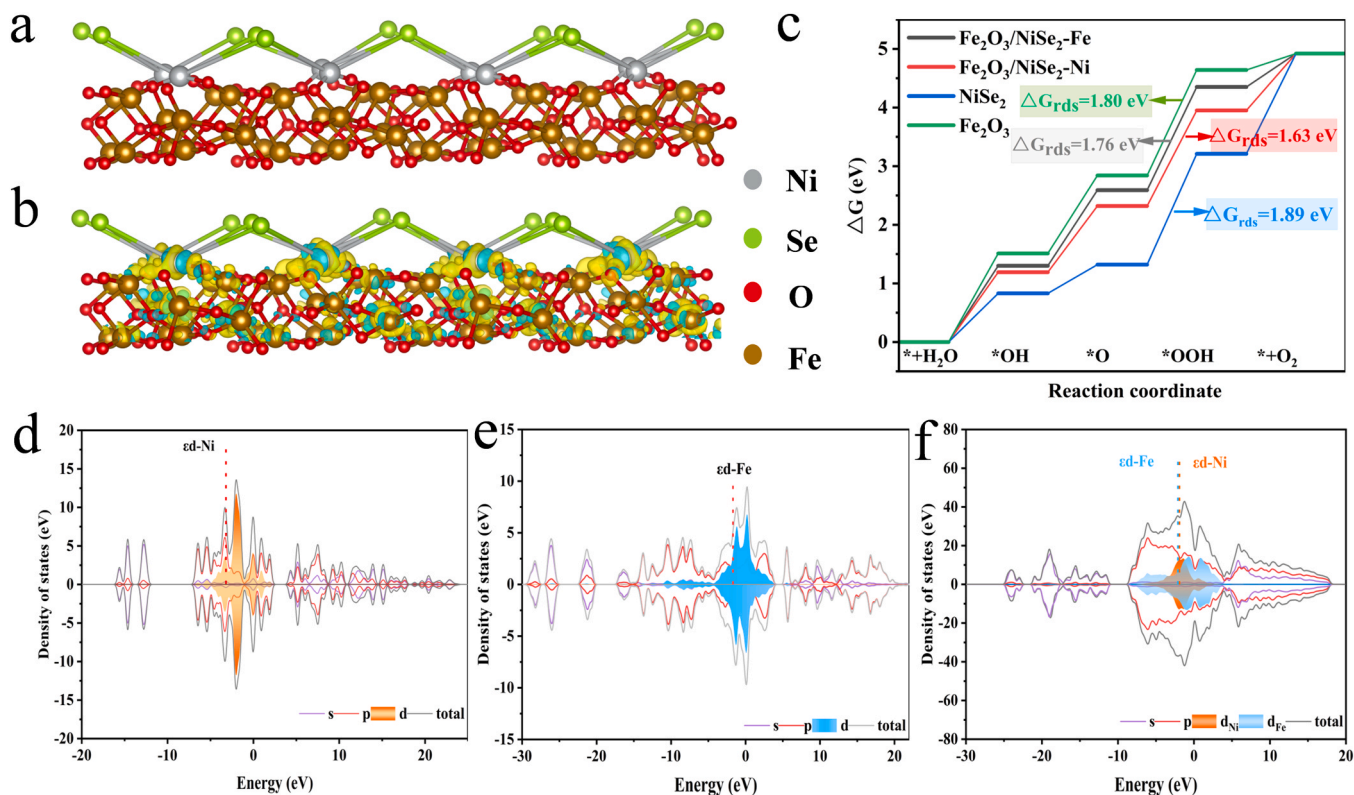
Fig. 5. (a) The optimized model of Fe₂O₃/NiSe₂. (b) The electron density difference of Fe₂O₃/NiSe₂ at the interface (the cyan and yellow regions represent electron depletion and accumulation, respectively). (c) OER free energy. The PDOS of (d) NiSe₂, (e) Fe₂O₃ and (f) Fe₂O₃/NiSe₂ heterojunction.

better insight into determining the real active intermediates and the reconstruction process of the catalysts. The collection voltage ranges from 1.12 V to 1.32 V. For NiSe₂/NF (Fig. 6a), there was no significant reconstruction observed on the catalyst surface when the potential was lower than 1.16 V. However, two peaks were detected at 468 and 558 cm⁻¹ at 1.16 V, which corresponded to the Ni-O (E_g) bending vibration mode and Ni-O ($A_{1\,g}$) stretching vibration mode of NiOOH [41], and the NiOOH peak intensity increases with potential, NiOOH intermediate is beneficial for OER. Additionally, the peak attributed to the

Se-Se bond (155 cm⁻¹) disappeared at 1.22 V, while a peak at 344 cm⁻¹ was attributed to characteristic vibration of amorphous selenide. Furthermore, a peak at 834 cm⁻¹ was observed, which was associated with selenic acid (SeO_4^-), the adsorption of selenate is beneficial for improving the OER process [42]. Interestingly, the adsorption peak of SeO_4^{2-} was not observed in Fe₂O₃/NiSe₂-FeOOH/NF (Fig. 6b) under the same test conditions, which is consistent with the results from ICP-MS (Table S6), Se-Se (218 cm⁻¹) experienced a shift to 209 cm⁻¹, which could be attributed to the contraction of the Ni-O bond upon the
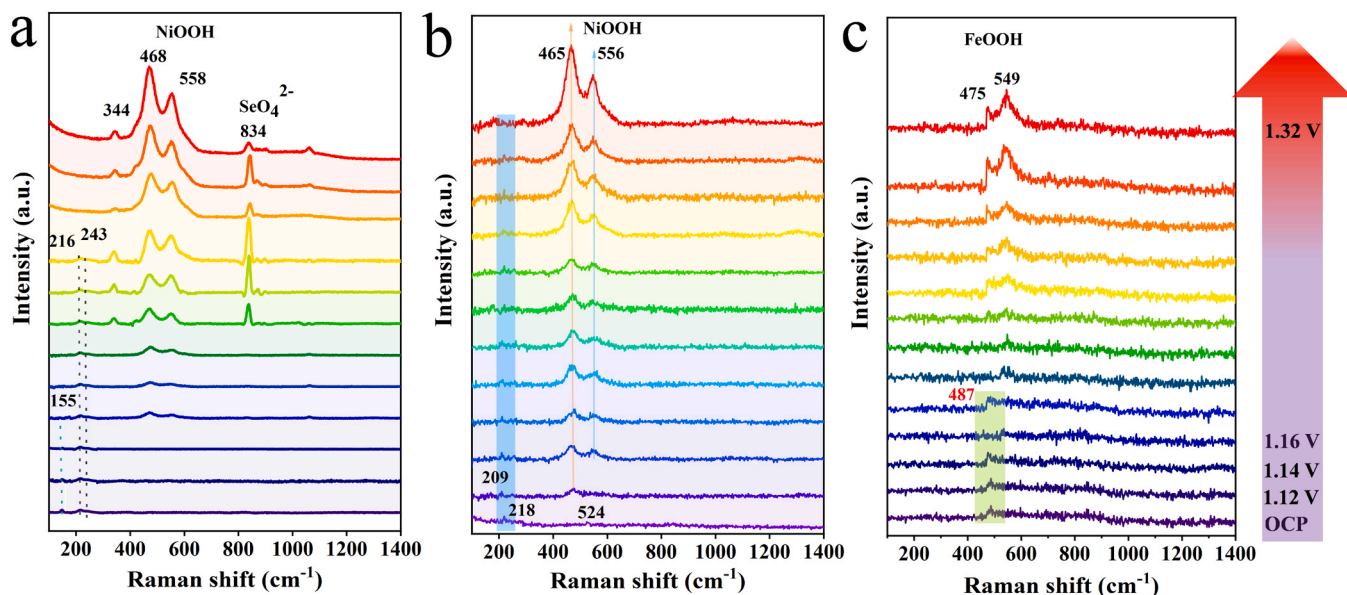

Fig. 6. In-situ Raman spectra of (a) NiSe₂/NF, (b) Fe₂O₃/NiSe₂-FeOOH/NF and (c) FeOOH/NF under the OER.

application of potential. NiOOH generation was detected at 1.12 V, which is lower than the potential of NiSe$_2$/NF (1.16 V) and the peak intensity increased with higher potential, indicating that the active site of Fe$_2$O$_3$/NiSe$_2$-FeOOH/NF is Ni. In general, the leaching of Se exposes more active sites, but the generated single hydroxide tends to aggregate during the reconstruction, while Fe$_2$O$_3$ in the Fe$_2$O$_3$/NiSe$_2$-FeOOH/NF acts as a nanofence, preventing the aggregation of NiOOH, this could be the reason for the high stability of the heterojunction in OER, which is consistent with many reports [43–45]. In-situ Raman spectroscopy was also used to detect the OER process of FeOOH/NF as a comparison (Fig. 6c), the result reveal a significantly lower Raman response intensity for FeOOH in comparison to the selenide. Under open-circuit potential conditions, a minor peak at 487 cm^{-1} was detected in the spectrum, which was attributed to the characteristic vibration of β-FeOOH [40]. Upon increasing the applied potential to 1.20 V, the peaks at 475 and 549 cm^{-1} were newly observed which be assigned to α-FeOOH [46,47] along with the disappearance of the β-FeOOH phase, indicating a change in the FeOOH phase during the electrochemical water oxidation.

4. Conclusions

In conclusion, we successfully loaded a dense heterojunction of Fe$_2$O$_3$/NiSe$_2$ onto FeOOH nanosheets. It shows an overpotential of 169 mV at 10 mA cm^{-2}, which is better than the most widely used IrO$_2$ catalyst and maintains good stability of industrially relevant current density (500 mA cm^{-2}). The high density of heterojunctions can be clearly observed by HRTEM, and a series of complementary spectra further expose the role of interface bonding in regulating the electronic state of the active site. DFT calculation reveals that electron redistribution at the interface not only improves the electrical conductivity of the heterojunction but also optimizes the adsorption energy of the intermediates. Moreover, in-situ Raman spectroscopy effectively tracked the reconstruction process of the catalyst in the OER, thereby furnishing crucial evidence for the authentic active site of the heterojunctions. It was worth noting that Fe$_2$O$_3$ components not only significantly improved the catalytic kinetics of Fe$_2$O$_3$/NiSe$_2$-FeOOH/NF through the interfacial interaction but also prevented the aggregation of active sites during the OER process. Finally, this study introduces a promising, cost-effective, and remarkable activity catalyst for OER and provides an achievable strategy for the exploration and design of more efficient heterostructured materials.

CRediT authorship contribution statement

Shuai Liu: Writing – original draft, Visualization, Validation, Methodology, Investigation, Formal analysis, Data curation, Conceptualization. **Fumin Wang:** Writing – review & editing, Investigation, Funding acquisition. **Xinyuan He:** Validation, Software, Methodology, Funding acquisition. **Tongxue Zhang:** Resources, Methodology, Formal analysis, Data curation. **Jiawei Wang:** Software, Resources, Methodology, Investigation. **Zheng Wang:** Validation, Supervision, Software, Investigation, Data curation. **Xijun Liu:** Writing – review & editing, Visualization, Validation, Formal analysis. **Xubin Zhang:** Writing – review & editing, Supervision, Software, Resources, Formal analysis, Conceptualization. **Zhiwei Zhang:** Validation, Supervision, Software, Project administration. **Qian Liu:** Visualization, Software, Formal analysis, Data curation.

Declaration of Competing Interest

The authors declare that they have no known competing financial interests or personal relationships that could have appeared to influence the work reported in this paper.

Data Availability

Data will be made available on request.

Appendix A. Supporting information

Supplementary data associated with this article can be found in the online version at doi:10.1016/j.apcatb.2024.124148.

References

[1] L.Q. Wang, L. Song, Z.Y. Yang, Y.M. Chang, F. Hu, L. Li, L.L. Li, H.Y. Chen, S. J. Peng, Electronic modulation of metal-organic frameworks by interfacial bridging for efficient ph-universal hydrogen evolution, Adv. Funct. Mater. 33 (2023) 2210322, https://doi.org/10.1002/adfm.202210322.

[2] S. Anantharaj, V. Aravindan, Developments and perspectives in 3d transition-metal-based electrocatalysts for neutral and near-neutral water electrolysis, Adv. Energy Mater. 10 (2019) 1902666, https://doi.org/10.1002/aenm.201902666.

[3] H. Liao, Y. Sun, C. Dai, Y. Du, S. Xi, F. Liu, L. Yu, Z. Yang, Y. Hou, A.C. Fisher, S. Li, Z.J. Xu, An electron deficiency strategy for enhancing hydrogen evolution on CoP nano-electrocatalysts, Nano Energy 50 (2018) 273–280, https://doi.org/10.1016/j.nanoen.2018.05.060.

[4] M.S. Burke, M.G. Kast, L. Trotochaud, A.M. Smith, S.W. Boettcher, Cobalt–iron (oxy)hydroxide oxygen evolution electrocatalysts: the role of structure and composition on activity, stability, and mechanism, J. Am. Chem. Soc. 137 (2015) 3638–3648, https://doi.org/10.1021/jacs.5b00281.

[5] H.G. SanchezCasalongue, M.L. Ng, S. Kaya, D. Friebel, H. Ogasawara, A. Nilsson, Insitu observation of surface species on iridium oxide nanoparticles during the oxygen evolution reaction, Angew. Chem. Int. Ed. 53 (2014) 7169–7172, https://doi.org/10.1002/anie.201402311.

[6] S. Hong, K. Ham, J. Hwang, S. Kang, M.H. Seo, Y.W. Choi, B. Han, J. Lee, K. Cho, Active motif change of Ni-Fe spinel oxide by ir doping for highly durable and facile oxygen evolution reaction, Adv. Funct. Mater. 33 (2022) 2209543, https://doi.org/10.1002/adfm.202209543.

[7] J. Liu, J. Xiao, Z. Wang, H. Yuan, Z. Lu, B. Luo, E. Tian, G.I.N. Waterhouse, Structural and electronic engineering of Ir-doped Ni-(Oxy)hydroxide nanosheets for enhanced oxygen evolution activity, ACS Catal. 11 (2021) 5386–5395, https://doi.org/10.1021/acscatal.1c00110.

[8] J. Shan, T. Ling, K. Davey, Y. Zheng, S.Z. Qiao, Transition-metal-doped ruir bifunctional nanocrystals for overall water splitting in acidic environments, Adv. Mater. 31 (2019) e1900510, https://doi.org/10.1002/adma.201900510.

[9] G. Huang, Z. Xiao, R. Chen, S. Wang, Defect engineering of cobalt-based materials for electrocatalytic water splitting, ACS Sustain. Chem. Eng. 6 (2018) 15954–15969, https://doi.org/10.1021/acssuschemeng.8b04397.

[10] M.Y. Ye, S. Li, X. Zhao, N.V. Tarakina, C. Teutloff, W.Y. Chow, R. Bittl, A. Thomas, Cobalt-exchanged poly(heptazine imides) as transition metal–Nx electrocatalysts for the oxygen evolution reaction, Adv. Mater. 32 (2020) 1903942, https://doi.org/10.1002/adma.201903942.

[11] S. Liu, M. Jin, J. Sun, Y. Qin, S. Gao, Y. Chen, S. Zhang, J. Luo, X. Liu, Coordination environment engineering to boost electrocatalytic CO2 reduction performance by introducing boron into single-Fe-atomic catalyst, Chem. Eng. J. 437 (2022) 135294, https://doi.org/10.1016/j.cej.2022.135294.

[12] X. Cao, Y. Hong, N. Zhang, Q. Chen, J. Masud, M.A. Zaeem, M. Nath, Phase exploration and identification of multinary transition-metal selenides as high-efficiency oxygen evolution electrocatalysts through combinatorial electrodeposition, ACS Catal. 8 (2018) 8273–8289, https://doi.org/10.1021/acscatal.8b01977.

[13] T.-P. Gao, K.W. Wong, K.M. Ng, Impacts of morphology and N-doped carbon encapsulation on electrochemical properties of NiSe for lithium storage, Energy Storage Mater. 25 (2020) 210–216, https://doi.org/10.1016/j.ensm.2019.10.013.

[14] L. Yang, X. Cao, X. Wang, Q. Wang, L. Jiao, Regulative electronic redistribution of CoTe2/CoP heterointerfaces for accelerating water splitting, Appl. Catal. B-Environ. 329 (2023) 122551, https://doi.org/10.1016/j.apcatb.2023.122551.

[15] Y.R. Pei, H.Y. Zhou, M. Zhao, J.C. Li, X. Ge, W. Zhang, C.C. Yang, Q. Jiang, High-efficiency sodium storage of Co$_{0.85}$Se/WSe$_2$ encapsulated in N-doped carbon polyhedron via vacancy and heterojunction engineering, Carbon Energy (2023) e374, https://doi.org/10.1002/cey2.374.

[16] J. Liu, S. Xiao, X. Li, Z. Li, X. Li, W. Zhang, Y. Xiang, X. Niu, J.S. Chen, Interface engineering of Fe3Se4/FeSe heterostructure encapsulated in electrospun carbon nanofibers for fast and robust sodium storage, Chem. Eng. J. 417 (2021) 129279, https://doi.org/10.1016/j.cej.2021.129279.

[17] Y. Yang, Y. Kang, H. Zhao, X. Dai, M. Cui, X. Luan, X. Zhang, F. Nie, Z. Ren, W. Song, An interfacial electron transfer on tetrahedral NiS$_2$/NiSe$_2$ heterocages with dual-phase synergy for efficiently triggering the oxygen evolution reaction, Small 16 (2019) 1905083, https://doi.org/10.1002/smll.201905083.

[18] X. Xu, J. Li, C. Zhang, S. Zhang, G. Su, Z. Shi, H. Wang, M. Huang, Controllable transition engineering from homogeneous NiSe₂ nanowrinkles to heterogeneous Ni3Se₄/NiSe₂ rod-like nanoarrays for promoted urea-rich water oxidation at large current densities, Appl. Catal. B-Environ. 319 (2022) 121949, https://doi.org/10.1016/j.apcatb.2022.121949.

[19] X. Zheng, X. Han, Y. Cao, Y. Zhang, D. Nordlund, J. Wang, S. Chou, H. Liu, L. Li, C. Zhong, Y. Deng, W. Hu, Identifying dense NiSe₂/CoSe₂ heterointerfaces coupled with surface high-valence bimetallic sites for synergistically enhanced oxygen electrocatalysis, Adv. Mater. 32 (2020) 2000607, https://doi.org/10.1002/adma.202000607.

[20] W. Li, L. Wu, X. Wu, C. Shi, Y. Li, L. Zhang, H. Mi, Q. Zhang, C. He, X. Ren, Regulation and mechanism study of the CoS₂/Cu₂S-NF heterojunction as highly-efficient bifunctional electrocatalyst for oxygen reactions, Appl. Catal. B-Environ. 303 (2022) 120849, https://doi.org/10.1016/j.apcatb.2021.120849.

[21] C. Zhu, A.L. Wang, W. Xiao, D. Chao, X. Zhang, N.H. Tiep, S. Chen, J. Kang, X. Wang, J. Ding, J. Wang, H. Zhang, H.J. Fan, In situ grown epitaxial heterojunction exhibits high-performance electrocatalytic water splitting, Adv. Mater. 30 (2018) 1705516, https://doi.org/10.1002/adma.201705516.

[22] J. Hu, A. Al-Salihy, J. Wang, X. Li, Y. Fu, Z. Li, X. Han, B. Song, P. Xu, Improved interface charge transfer and redistribution in CuO-CoOOH p-n heterojunction nanoarray electrocatalyst for enhanced oxygen evolution reaction, Adv. Sci. 8 (2021) 2103314, https://doi.org/10.1002/advs.202103314.

[23] P.L. Zhai, Y.X. Zhang, Y.Z. Wu, J.F. Gao, B. Zhang, S.Y. Cao, Y.T. Zhang, Z.W. Li, L. C. Sun, J.G. Hou, Engineering active sites on hierarchical transition bimetal oxides/sulfides heterostructure array enabling robust overall water splitting, Nat. Commun. 11 (2020) 5462, https://doi.org/10.1038/s41467-020-19214-w.

[24] L. An, Y. Li, M. Luo, J. Yin, Y.Q. Zhao, C. Xu, F. Cheng, Y. Yang, P. Xi, S. Guo, Atomic-level coupled interfaces and lattice distortion on CuS/NiS2 nanocrystals boost oxygen catalysis for flexible Zn-air batteries, Adv. Funct. Mater. 27 (2017) 1703779, https://doi.org/10.1002/adfm.201703779.

[25] C.C.L. McCrory, S. Jung, J.C. Peters, T.F. Jaramillo, Benchmarking heterogeneous electrocatalysts for the oxygen evolution reaction, J. Am. Chem. Soc. 135 (2013) 16977–16987, https://doi.org/10.1021/ja407115p.

[26] J. Kwon, H. Han, S. Jo, S. Choi, K.Y. Chung, G. Ali, K. Park, U. Paik, T. Song, Amorphous nickel-iron borophosphate for a robust and efficient oxygen evolution reaction, Adv. Energy Mater. 11 (2021) 2100624, https://doi.org/10.1002/aenm.202100624.

[27] H. Sun, L. Chen, Y. Lian, W. Yang, L. Lin, Y. Chen, J. Xu, D. Wang, X. Yang, M. H. Rummerli, J. Guo, J. Zhong, Z. Deng, Y. Jiao, Y. Peng, S. Qiao, Topotactically transformed polygonal mesopores on ternary layered double hydroxides exposing under-coordinated metal centers for accelerated water dissociation, Adv. Mater. 32 (2020) 2006784, https://doi.org/10.1002/adma.202006784.

[28] C. Tang, N. Cheng, Z. Pu, W. Xing, X. Sun, NiSe nanowire film supported on nickel foam: an efficient and stable 3D bifunctional electrode for full water splitting, Angew. Chem. Int. Ed. 54 (2015) 9351–9355, https://doi.org/10.1002/anie.201503407.

[29] B.J. Taitt, D.-H. Nam, K.-S. Choi, A comparative study of Nickel, Cobalt, and iron oxyhydroxide anodes for the electrochemical oxidation of 5-hydroxymethylfurfural to 2,5-furandicarboxylic acid, ACS Catal. 9 (2018) 660–670, https://doi.org/10.1021/acscatal.8b04003.

[30] L. Zhai, T.W.B. Lo, Z.-L. Xu, J. Potter, J. Mo, X. Guo, C.C. Tang, S.C.E. Tsang, S. P. Lau, In situ phase transformation on nickel-based selenides for enhanced hydrogen evolution reaction in alkaline medium, ACS Energy Lett. 5 (2020) 2483–2491, https://doi.org/10.1021/acsenergylett.0c01385.

[31] Z.-W. Gao, J.-Y. Liu, X.-M. Chen, X.-L. Zheng, J. Mao, H. Liu, T. Ma, L. Li, W.-C. Wang, X.-W. Du, Engineering NiO/NiFe LDH intersection to bypass scaling relationship for oxygen evolution reaction via dynamic tridimensional adsorption of intermediates, Adv. Mater. 31 (2019) 1804769, https://doi.org/10.1002/adma.201804769.

[32] Y. Li, Y. Wu, H. Hao, M. Yuan, Z. Lv, L. Xu, B. Wei, Operando spectroscopies unveil interfacial FeOOH induced highly reactive β-Ni(Fe)OOH for efficient oxygen evolution, Appl. Catal. B-Environ. 318 (2022) 121825, https://doi.org/10.1016/j.apcatb.2022.121825.

[33] L. Wang, X. Wang, S. Xi, Y. Du, J. Xue, alpha-Ni(OH)(2) originated from electro-oxidation of NiSe(2) supported by carbon nanoarray on carbon cloth for efficient water oxidation, Small 15 (2019) e1902222, https://doi.org/10.1002/smll.201902222.

[34] G. Shen, R. Zhang, L. Pan, F. Hou, Y. Zhao, Z. Shen, W. Mi, C. Shi, Q. Wang, X. Zhang, J.J. Zou, Regulating the spin state of Fe(III) by atomically anchoring on ultrathin titanium dioxide for efficient oxygen evolution electrocatalysis, Angew. Chem. Int. Ed. Engl. 59 (2020) 2313–2317, https://doi.org/10.1002/anie.201913080.

[35] C.-Y. Moon, H. Kang, B.G. Jang, J.H. Shim, Composition and temperature dependent electronic structures of NiS₂₋ₓSeₓ alloys: first-principles dynamical mean-field theory approach, Phys. Rev. B 92 (2015) 235130, https://doi.org/10.1103/PhysRevB.92.235130.

[36] Y. Sun, S. Sun, H. Yang, S. Xi, J. Gracia, Z.J. Xu, Spin-related electron transfer and orbital interactions in oxygen electrocatalysis, Adv. Mater. 32 (2020), https://doi.org/10.1002/adma.202003297.

[37] Z. Xu, Y. Ying, G. Zhang, K. Li, Y. Liu, N. Fu, X. Guo, F. Yu, H. Huang, Engineering NiFe layered double hydroxide by valence control and intermediate stabilization toward the oxygen evolution reaction, J. Mater. Chem. A 8 (2020) 26130–26138, https://doi.org/10.1039/d0ta08815c.

[38] L. Jiang, N. Yang, C. Yang, X. Zhu, Y. Jiang, X. Shen, C. Li, Q. Sun, Surface wettability engineering: CoSx-Ni3S2 nanoarray electrode for improving overall water splitting, Appl. Catal. B-Environ. 269 (2020) 118780, https://doi.org/10.1016/j.apcatb.2020.118780.

[39] X. Xu, F. Song, X. Hu, A nickel iron diselenide-derived efficient oxygen-evolution catalyst, Nat. Commun. 7 (2016) 12324, https://doi.org/10.1038/ncomms12324.

[40] J.X. Feng, H. Xu, Y.T. Dong, S.H. Ye, Y.X. Tong, G.R. Li, FeOOH/Co/FeOOH hybrid nanotube arrays as high-performance electrocatalysts for the oxygen evolution reaction (vol 55, pg 3694, 2016), Angew. Chem. Int. Ed. 58 (2019), https://doi.org/10.1002/anie.201908187, 14795-14795.

[41] M. Chen, Y. Zhang, R. Wang, B. Zhang, B. Song, Y. Guan, S. Li, P. Xu, Surface reconstruction of Se-doped NiS₂ enables high-efficiency oxygen evolution reaction, J. Energy Chem. 84 (2023) 173–180, https://doi.org/10.1016/j.jechem.2023.05.009.

[42] Y. Shi, W. Du, W. Zhou, C. Wang, S. Lu, S. Lu, B. Zhang, Unveiling the promotion of surface-adsorbed chalcogenate on the electrocatalytic oxygen evolution reaction, Angew. Chem. Int. Ed. 59 (2020) 22470–22474, https://doi.org/10.1002/anie.202011097.

[43] Y.J. Son, S. Kim, V. Leung, K. Kawashima, J. Noh, K. Kim, R.A. Marquez, O. A. Carrasco-Jaim, L.A. Smith, H. Celio, D.J. Milliron, B.A. Korgel, C.B. Mullins, Effects of electrochemical conditioning on nickel-based oxygen evolution electrocatalysts, ACS Catal. 12 (2022) 10384–10399, https://doi.org/10.1021/acscatal.2c01001.

[44] K. Wang, H. Du, S. He, L. Liu, K. Yang, J. Sun, Y. Liu, Z. Du, L. Xie, W. Ai, W. Huang, Kinetically controlled, scalable synthesis of gamma-FeOOH nanosheet arrays on nickel foam toward efficient oxygen evolution: the key role of in-situ-generated gamma-NiOOH, Adv. Mater. 33 (2021) e2005587, https://doi.org/10.1002/adma.202005587.

[45] Q. Ji, Y. Kong, H. Tan, H. Duan, N. Li, B. Tang, Y. Wang, S. Feng, L. Lv, C. Wang, F. Hu, W. Zhang, L. Cai, W. Yan, Operando identification of active species and intermediates on sulfide interfaced by Fe₃O₄ for ultrastable alkaline oxygen evolution at large current density, ACS Catal. 12 (2022) 4318–4326, https://doi.org/10.1021/acscatal.2c01090.

[46] Y. Li, Y. Wu, H. Hao, M. Yuan, Z. Lv, L. Xu, B. Wei, In situ unraveling surface reconstruction of Ni₅P₄@FeP nanosheet array for superior alkaline oxygen evolution reaction, Appl. Catal. B-Environ. 305 (2022) 121033, https://doi.org/10.1016/j.apcatb.2021.121033.

[47] J. Ge, J.Y. Zheng, J. Zhang, S. Jiang, L. Zhang, H. Wan, L. Wang, W. Ma, Z. Zhou, R. Ma, Controllable atomic defect engineering in layered NixFe1−x(OH)2 nanosheets for electrochemical overall water splitting, J. Mater. Chem. A 9 (2021) 14432–14443, https://doi.org/10.1039/d1ta02188e.